

pubs.acs.org/JACS Article

Exploration of the Solid-State Sorption Properties of Shape-Persistent Macrocyclic Nanocarbons as Bulk Materials and Small Aggregates

Tobias A. Schaub,* Ephraim A. Prantl, Julia Kohn, Markus Bursch, Checkers R. Marshall, Erik J. Leonhardt, Terri C. Lovell, Lev N. Zakharov, Carl K. Brozek, Siegfried R. Waldvogel, Stefan Grimme, and Ramesh Jasti*



Cite This: J. Am. Chem. Soc. 2020, 142, 8763-8775



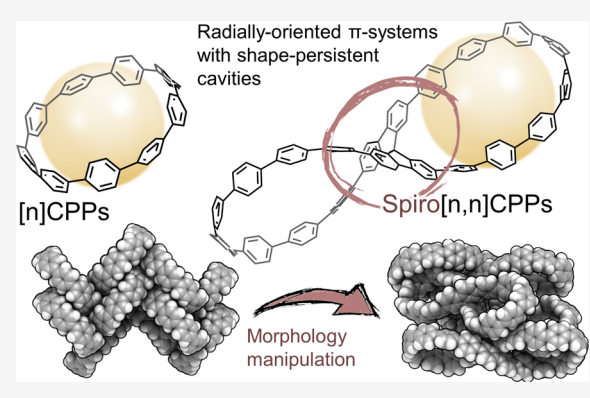
ACCESS

Metrics & More



Supporting Information

ABSTRACT: Porous molecular materials combine benefits such as convenient processability and the possibility for atom-precise structural fine-tuning which makes them remarkable candidates for specialty applications in the areas of gas separation, catalysis, and sensing. In order to realize the full potential of these materials and guide future molecular design, knowledge of the transition from molecular properties into materials behavior is essential. In this work, the class of compounds termed cycloparaphenylenes (CPPs)—shape-persistent macrocycles with built-in cavities and radially oriented π -systems—was selected as a conceptually simple class of intrinsically porous nanocarbons to serve as a platform for studying the transition from analyte sorption properties of small aggregates to those of bulk materials. In our detailed investigation, two series of CPPs were probed: previously reported hoop-shaped [n]CPPs and a novel family of all-phenylene figure-8 shaped (lemniscal)



bismacrocycles, termed spiro [n,n] CPPs. A series of nanocarbons with different macrocycle sizes and heteroatom content have been prepared by atom-precise organic synthetic methods, and their structural, photophysical, and electronic attributes were disclosed. Detailed experimental studies (X-ray crystallography, gas sorption, and quartz-crystal microbalance measurements) and quantum chemical calculations provided ample evidence for the importance of the solid-state arrangement on the porosity and analyte uptake ability of intrinsically porous molecular nanocarbons. We demonstrate that this molecular design principle, i.e., incorporation of sterically demanding spiro junctions into the backbone of nanohoops, enables the manipulation of solid-state morphology without significantly changing the nature and size of the macrocyclic cavities. As a result, the novel spiro [n,n] CPPs showed a remarkable performance as high affinity material for vapor analyte sensing.

1. INTRODUCTION

Porous carbonaceous materials are key components for the development of next-generation technologies in the fields of separation technologies,^{1–3} heterogeneous catalysis,^{4–6} and energy storage.^{7–10} To achieve specific device applications, a current objective of intense research is to obtain a better understanding of the parameters that dictate the interactions of porous matter with its environment—most often small molecular analytes, ions, liquids, or gases.^{11–13} In order to improve performances, pore/size distribution, surface areas,^{14–16} as well as the physicochemical microenvironment of the pores^{1,17,18} need to be considered and ultimately adjusted in an atomically precise fashion. In this context, porous materials composed of discrete molecular nanocarbons represent ideal candidates to systematically study fundamental structure/property relationships as the pore information can be directly encoded into the molecular framework.^{19–21} Two fundamen-

tally disparate categories of porosity can be distinguished: (i) extrinsic porosity wherein interstitial void space is generated between suitably designed compounds and (ii) prefabricated cavities built into the isolated molecular building blocks, i.e., intrinsic porosity. ²⁰ Realizing permanent and accessible pores in the solid state is a challenging task since not only the molecular scaffolds need to be rigid enough to avoid structural collapse upon solvent removal but also the compound must assemble in a way that the built-in cavity remains accessible.

Received: February 4, 2020 Published: April 11, 2020





For hoop-shaped macrocyclic structures—the most simple intrinsically porous objects—pore accessibility represents a key challenge. Depending on the crystallization conditions, various types of packing can be achieved including layer-, channel-, and herringbone-type arrangements.²² The type of solid-state packing is decisive for the porous nature of the obtained molecular materials; in herringbone-type assemblies, for instance, the available pore space has been reported to be significantly reduced due to self-filling cavities.²³ A paradigmatic example in this respect are cycloparaphenylenes (CPPs)^{24–26} which predominantly adopt a herringbone-type arrangement, but also the classes of cyclodextrins (CD),^{27–30} cucurbiturils (CB),^{31,32} and Anderson's porphyrin nanorings³³ have been reported to display this packing motif (Figure 1).

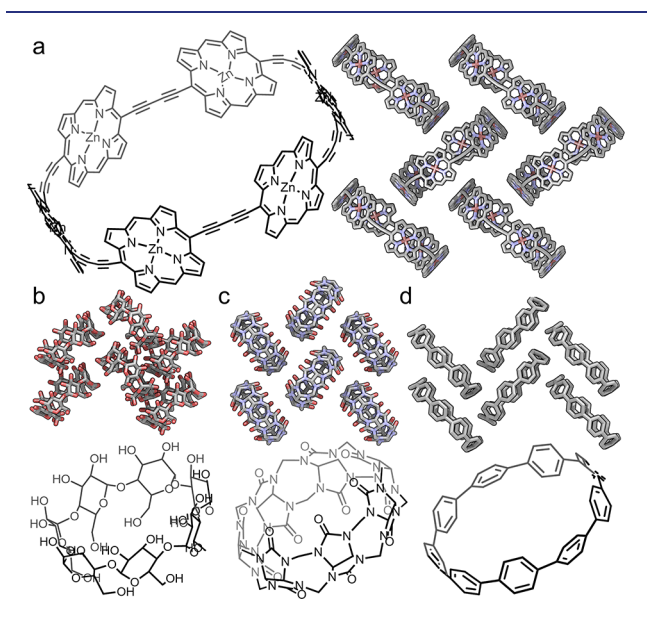


Figure 1. Illustration of the herringbone packing of selected nanorings: porphyrin nanoring (substituents omitted, a), ²³ β-CD (b), ³⁰ CB[7] (c), ²⁹ and [9]CPP (d). ³²

Being composed entirely of aromatic phenylene rings, we speculated that the fascinating class of CPPs³⁴⁻³⁷—shapepersistent macrocyclic nanocarbons—provides a unique opportunity to manipulate solid-state arrangements by molecular design while maintaining the molecular properties, i.e., the radially oriented π -systems and macrocyclic cavity sizes. By changing the connectivity of the phenylene units in hoop-shaped [n]CPPs, a new family of all-phenylene lemniscal nanocarbons, spiro[n-n]CPPs, ^{38,39} was prepared in which two macrocycles are fused in a central spiro-motif. With these novel macrocycles in hand, we were able to explore the impact on sorption and analyte uptake performance of preparing CPP compounds as either small aggregates versus bulk solids through a suite of X-ray crystallography, gas sorption, and quartz-crystal microbalance (QCM)-based analyte sensing measurements. The experimental results were supported by quantum chemical density functional theory (DFT) calculations that unveiled the energy and porosity landscape associated with these new affinity materials. Our analysis indicates that the impact of molecular shapes and sizes on supramolecular and bulk functional behavior may be at times counterintuitive, rich, and complex, therefore deserving careful case-by-case analysis to deepen our understanding of the intermolecular chemistry that produces porous molecular matter.

2. RESULTS AND DISCUSSION

2.1. Molecular Geometry Predictions. To get an impression of the molecular dimensions and internal cavity sizes of lemniscal macrocycles 1–3, initially, their geometry-optimized structures were calculated using dispersion-corrected Kohn–Sham DFT calculations (TPSS-D3(BJ)^{40–43}/def2-TZVP, ⁴⁴ gas-phase) (Figure 2, top). All compounds adopt the

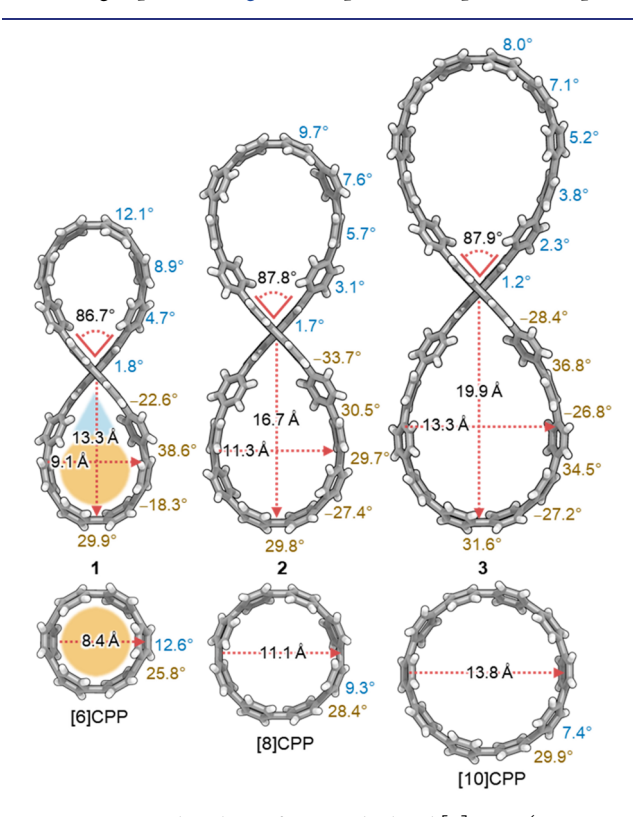


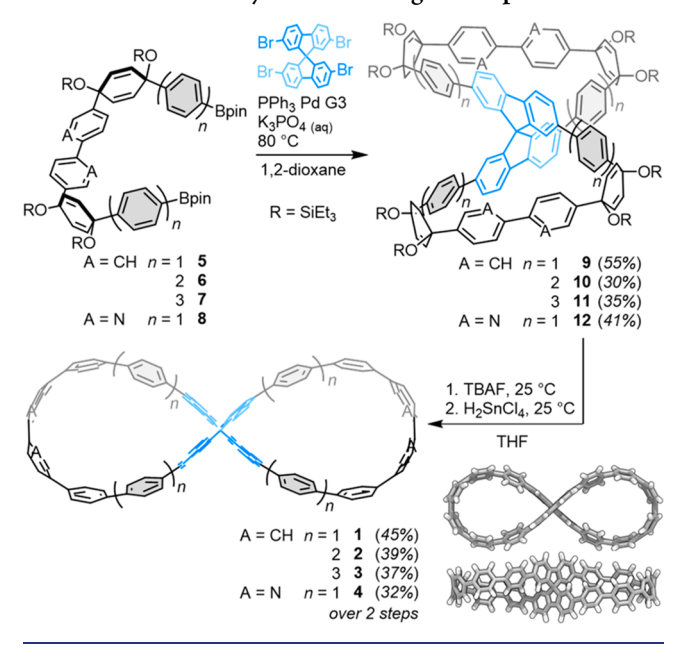
Figure 2. Structural analysis of 1-3 and related [n] CPPs (n=6,8,10, TPSS-D3/def2-TZVP, gas phase): molecular dimensions (black), mean boat angle of individual phenyl rings (blue), and phenylene torsion angles (yellow). Only P-enantiomers are shown for 1-3.

expected figure-8 shape in which the spiro-motif is enforcing a contiguous D2-symmetric geometry. While stereochemical aspects are beyond the scope of this study, it is worth noting the configurationally stable chirality of compounds 1-3 in which inversion is prohibited by the rigid sp³-hybridized carbon of the central stereogenic spiro motif. The rigidity of the spiro center is reflected in the virtually ideal rectangular dihedral angle between two 9,9'-fluorene halves for compounds 1-3 (86.7°-87.9°) as compared to Stepień's recently published lemniscate (70.9°), ³⁸ featuring a 9,9′-bicarbazole unit as the central motif which allows for N-N single-bond rotation. For [n]CPPs, macrocycle size is the key factor that governs the inherent strain and consequently the structural parameter along the phenylene backbone. 45 Unsurprisingly, lemniscal structures behave similarly in that the strain enthalpy (estimated by homodesmotic reactions, see the Supporting Information, Scheme S1)⁴⁶ increases from 2.6 kcal/mol per phenyl ring (total 61.8 kcal/ mol) for 3 over 3.7 kcal/mol (total 73.1 kcal/mol) for 2, to 5.8 kcal/mol (total 92.2 kcal/mol) for 1, i.e., with decreasing macrocycle size. This strain is not equally distributed over the phenylene backbone. As a consequence, the phenyl ring boat angles steadily increase (i) with segment curvature, i.e., from the spiro center $(1.2^{\circ}-1.8^{\circ})$ to the outer nanoloop turning points

 $(8.0^\circ-12.1^\circ)$, and (ii) with decreasing macrocycle size from 3 $(1.2^\circ-8.0^\circ)$ to 1 $(1.8^\circ-12.1^\circ)$. Similarly, the mean phenylene torsion angles are generally found to increase with macrocycle size from 1 (27.4°) , to 2 (30.2°) , and 3 (30.8°) . The main part of the cavity of lemniscates 1–3 is formed by the outer phenylene backbone and largely resembles that of [6]-, [8]-, and [10]CPP in size and nature, respectively (Figure 2, bottom). He addition, the lemniscate series provide a V-shaped void space in the vicinity of the spiro center (blue triangle) as compared to [n]CPPs.

2.2. Synthesis. We commnced our synthetic efforts toward hydrocarbon lemniscate 1 using "C"-shaped building block 5 as a coupling partner in the double macrocyclization with commercially available 2,2',7,7'-tetrabromo-9,9'-spirobifluorene (Scheme 1). Similar to the recently published 9,9'-

Scheme 1. Modular Synthesis of Target Compounds 1-4



bicarbazole derivative, ³⁸ the ideal size and shape fit of coupling partners were reflected in a remarkable 55% yield for the formation of compound 9 considering the generation of two macrocycles in a single step. Macrocycle 9 was quantitatively deprotected and subsequently subjected to the H2SnCl4mediated reductive aromatization conditions reported by Yamago⁴⁷ to give the all-hydrocarbon target compound 1. Similarly, we were able to access larger macrocycles 10 and 11 by extending compound 5 at the phenyl termini via a Suzuki coupling/borylation sequence to prepare 8-ring 6 and 10-ring coupling partner 7. After deprotection and reductive aromatization, larger lemniscates 2 and 3 were obtained in moderate yields. To explore the possibility to tune the molecular and materials properties by subtle modifications of the scaffold, we prepared nitrogen-containing bis(bipyridyl) derivative 4 in a like manner by employing bipyridyl coupling partner 8 (for detailed synthetic procedures, see the Supporting Information). All figure-8 nanohoops 1-4 were obtained as fine powders that can be stored at ambient conditions for months without spectroscopically traceable decomposition. The structures of compounds 1-4 were determined using NMR spectroscopy, mass spectrometry, and, in the case of compounds 1, 2, and 4, by single-crystal X-ray diffraction.

2.3. Photophysical and Electronic Characterization. In the following, a brief discussion of the optoelectronic properties of **1–4** is provided. For more details, we refer the reader to the Supporting Information. A thorough study of the chiroptical properties of a 9,9'-bicarbazole lemniscate was recently published.³⁸ The electronic absorption and emission spectra of compounds **1–4** were recorded in CH₂Cl₂ at room temperature (Figure 3a, see also Table 1). Hydrocarbons **1–3**

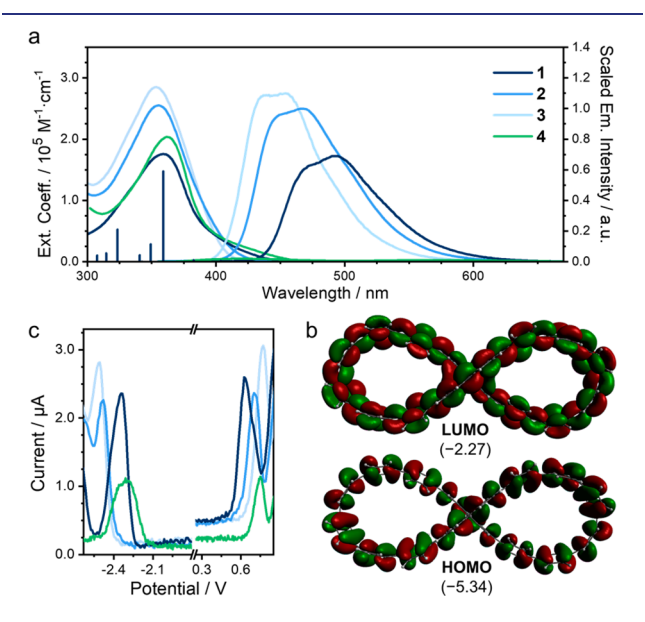


Figure 3. Electronic absorption and emission spectra in CH_2Cl_2 at rt along with the oscillator strengths (only shown for 1, blue bars) obtained by TD-DFT calculations (TD-B3LYP/def2TZVP, a); exemplary Kohn–Sham FMOs of 1 (0.01 au isosurfaces, b); and differential pulse voltammogram of 1–4 (in THF + 0.1 NBu₄PF₆, vs Fc/Fc⁺, c).

Table 1. Photophysical and Electrochemical Data of the Title Compounds (for Details on the Measurements Conditions see the Supporting Information)

	$\lambda_{\rm max}/{\rm nm}$, $\varepsilon/10^5~{\rm M}^{-1}{\cdot}{\rm cm}^{-1}$	$\lambda_{\rm em}/{\rm nm}$	Φ/au	$E_{\rm ox}/{ m V}$	$E_{\rm red}/{ m V}$
1	359 (1.76)	493	0.37	0.63	-2.34
2	355 (2.55)	468	0.64	0.71	-2.48
3	353 (2.85)	454	0.86	0.77	-2.51
4	363 (2.03)	n/a^a	n/a ^a	0.76	-2.30
^a Compound 4 is not emissive in solution.					

share a common absorption band in the near-UV/vis region $(\lambda_{\text{max}} = 353-358 \text{ nm})$, which is red-shifted compared to the [n]CPP series ($\lambda_{\text{max}} = 335 - 340 \text{ nm}$). The extinction coefficients reach up to $2.85 \pm 0.05 \times 10^5 \text{ M}^{-1} \cdot \text{cm}^{-1}$ for 3, which is approximately twice the extinction coefficient of similarly sized [n]CPP (n = 12, $\varepsilon = 1.2 - 1.4 \times 10^5 \text{ M}^{-1} \cdot \text{cm}^{-1}$).⁴⁸ Our timedependent (TD) DFT calculations for 1-3 indicate that the absorption bands are composed of HOMO $-2 \rightarrow LUMO$ and, more pronounced, HOMO \rightarrow LUMO+2 transitions (S₃, f =3.24-5.65; for 4: f = 2.12), respectively (Figure 3b, Supporting Information Tables S9–S12). HOMO \rightarrow LUMO (S1, f =0.012-0.047; for 4: f = 0.131) as well as HOMO-1 \rightarrow LUMO and HOMO \rightarrow LUMO+1 (S₂, f = 0.016 - 0.051; for 4: f = 0.077) excitations for 1-4 are only weakly allowed, which is reflected in the observed weak absorption band shoulders in the visible region, respectively. The TD-DFT results also reproduce the observed slight red-shift of the absorption maximum with decreasing macrocycle size, i.e., from 3 to 1, which results from a relative destabilization of the HOMO (Figure 3b) over the LUMO+2 energy level, in which the electron density is shifted toward the central spiro motif (see the Supporting Information, Figure S52). The observed red-shifting fluorescence and rapid decrease in quantum efficiency with smaller macrocycle sizes are characteristic features for CPP-derived macrocycles; a fundamental explanation of these strain- and symmetry-related phenomena has been provided by Tretiak. 49 In the experiment, the fluorescence of compound 4 is completely quenched in solution (see Figure 3a) in contradiction to previous observations which reported that embedded nitrogen atoms have little impact on the electronic structure of CPP-based nanohoops.²⁸ A detailed investigation of the apparently different excited-state relaxation mechanisms of compounds 1 and 4, however, exceeds the scope of this study. The electrochemical characteristics of the target compounds were studied by cyclic voltammetry (see the Supporting Information, Figure S51) and differential pulse voltammetry in 0.1 M NBu₄PF₆ in THF solution and the measured redox potentials referenced vs ferrocene/ferrocenium+ (Fc/Fc+, Figure 3c, Table 1). All compounds exhibit quasi-reversible reduction and oxidation events. We observe a widening of the electrochemical gap with macrocycle size (1: 2.97 eV, 2: 3.19 eV, 3: 3.28 eV), which is caused by a simultaneous shift of the first oxidation/reduction to more positive/negative potentials, respectively. This increase in the electrochemical band gap is well documented for [n] CPPs;⁴ for instance, in their oxidation potentials, compounds 1-3 resemble those of [8]- (0.59 eV), [9]- (0.70 eV), and [10]CPP (0.74 eV),⁵⁰ and the simultaneous shift to more negative reduction potentials with increasing macrocycle size has been documented experimentally for [5]- $(-2.27 \text{ eV})^{51}$ and [7]CPP (-2.74 eV)⁵² as well as theoretically.⁵⁰ Comparison of bis(bipyridyl)-substituted 4 with its closely related all-phenylene relative 1 reveals slightly more positive reduction ($\Delta E_{\text{red}} = 0.04$ eV) and oxidation potentials ($\Delta E_{\rm ox} = 0.13$ eV), indicating an opportunity to tune the frontier molecular orbital (FMO) energies by subtle structural modifications such as heteroatom incorporation.

2.4. Bulk Sorption and Crystal Structures. Next, we investigated how structural and electronic differences between these molecules lead to molecular packing arrangements that determine the bulk structures. First, the presence and shape of micropores were probed by acquiring N2 uptake isotherms for compounds 1-3 (Figure 4). Compound 2 shows appreciable N₂ uptake at 77 K. High quantities of N2 were absorbed at low relative pressures, indicating that 2, assembled in bulk form, exhibits microporosity (Figure S37). Brunauer-Emmett-Teller (BET) analysis was performed on these data to give a specific surface area of 703 m²·g⁻¹. The high gas uptake of this sample is consistent with its low crystallographic density and high accessible unit cell volume, as well as how the powder maintains crystallinity in extreme evacuation conditions. The N₂ isotherms of compounds 1 and 3 show rather low N2 uptake and surface areas of 33.9 m²·g⁻¹ and 11.8 m²·g⁻¹, respectively. This may be due to a lack of long-range order as seen by PXRD since pore access relies on crystal packing. The product 3 is amorphous, lacking long-range order even before the evacuation (see the Supporting Information, Figure S41). Although the increasing accessible unit cell volume from [9]CPP to [12]CPP observed by crystallography indicates that materials with large macrocycle size have more accessible pore space (vide infra),

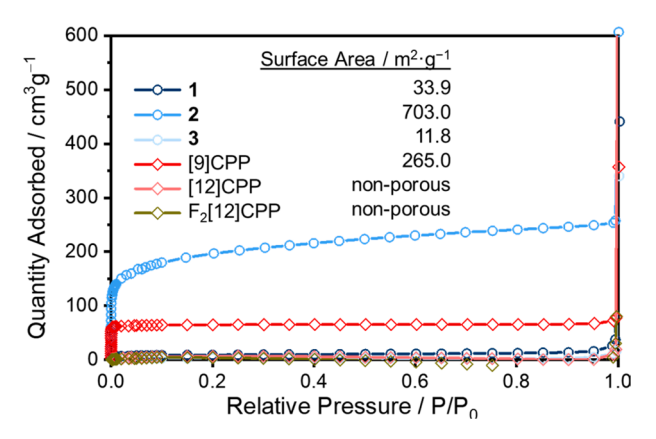


Figure 4. N₂ uptake isotherms collected at 77 K and calculated surface areas (for details on the sample preparation see the Supporting Information).

their gas uptake does not follow this trend. It is important to note that the bulk material will exhibit differing long-range order compared to its single-crystal analogue. Before and after evacuation, [9]CPP exhibits well-defined diffraction peaks, while [12] CPP loses much of its long-range order. N2 uptake measurements on [9]CPP yield a BET surface area of 265 m^2 · g⁻¹, while the BET surface area of both [12]CPP and F₂-[12]CPP is negligible. A previous study on [12]CPP could show that notable N2 uptake was only observed at increased temperatures of approximately 195 K, indicating thermal vibrations and molecular motions to be crucial in cases where hoop-shaped molecules in the bulk solid pack to block one another's intrinsic pores.²³ In this context, the lemniscate family may have an advantage in the more randomly oriented powder material, as the built-in cavities and much of the interstitial space in the unit cell volume are left accessible. In contrast, the [n]CPP family preferably arranges in tightly packed hexagonal nanochannels that could be easily "sealed" by a single self-closing cavity. A similar effect was reported for the series of hoop-shaped $\operatorname{cucurbit}[n]$ urils, where self-closing of the built-in cavities was found to influence the propensity for guest uptake and release.³¹

We were able to obtain single crystals for compounds 1, 2, and 4 suitable for X-ray crystallographic analysis (Figure 5a, for more details see the Supporting Information).⁵³ Single crystals were grown by slow liquid diffusion of pentane into a solution of 1 (in CHCl₃, 25 °C), 2 (in CH₂Cl₂, 25 °C), and 4 (in THF, 7 °C) for several days, respectively. Our data not only unambiguously prove the molecular structure of 1, 2, and 4 and corroborate our computational geometry prediction but also put us in a position to study the solid-state packing of these unique macrocyclic architectures. Most strikingly, the dense herringbone-type arrangement characteristic for [n]CPPs is not observed for hydrocarbon lemniscates 1 and 2, and instead a less ordered and more loosely packed supramolecular arrangement is adopted. This situation is best reflected in a decrease of the average number of short contacts per phenyl ring—dictated by weak to moderate CH $-\pi$ and π - π interactions—in the order [9]CPP $(3.8) > [12]CPP(3.2) > 1 \approx 2 (2.3, Figure 5b)$. In other words, $\lceil n \rceil$ CPPs are held in place more tightly within the crystal lattice compared to the lemniscate series. In addition, the incorporation of the spiro motif in the lemniscates minimizes the molecular surface consumed for intermolecular contacts, leaving interstitial space as well as the built-in cavities more accessible. This picture is quite in contrast to the parent [n]CPPs, which typically self-assemble into staggered, herringbone-like packing

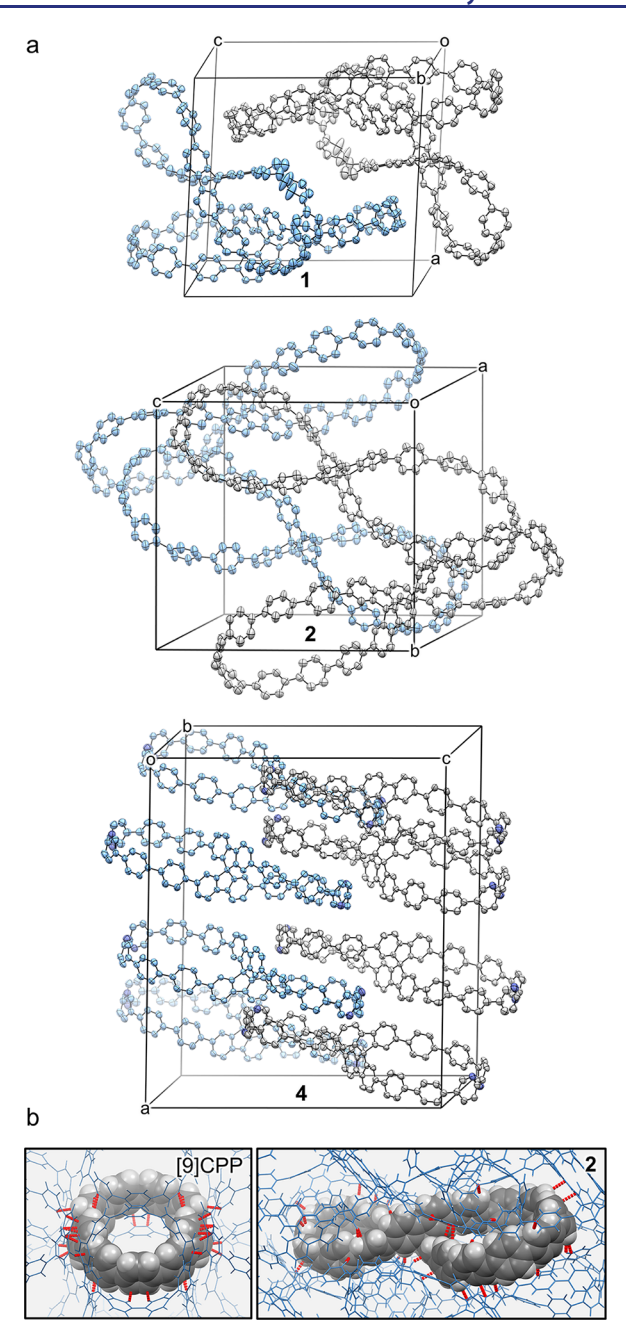


Figure 5. Unit cell of 1, 2, and 4 determined by X-ray crystallography (50% probability level, solvent molecules and hydrogens are omitted, (M) enantiomers colored in blue for clarity, a). Short contacts for [9] CPP (3.8 per phenyl ring) and lemniscate 2 (2.3 per phenyl ring, b).

motifs which minimizes intrinsic cavity and interstitial void space. ^{24,25} Replacement of phenyl carbons by nitrogens in compound 4 enforces a supramolecular packing reminiscent of an interdigitating slipped stack arrangement of the macrocyclic loops of alternating enantiomers (Figure S36). Apart from weak CH··· π interactions, two dominant intermolecular interactions are found in the crystal structure: (i) π – π stacking between a phenyl and a pyridyl ring and (ii) supramolecular CH···N interactions (3.60–3.88 Å) of the pyridyl nitrogen lone pairs with adjacent phenyl rings.

The pore structure and crystallographic parameters of the newly synthesized materials were compared to the parent series of [n]CPPs $(n = 6,^{54} 9,^{26} \text{ and } 12,^{55} \text{ Figure } 6)$. Additionally,

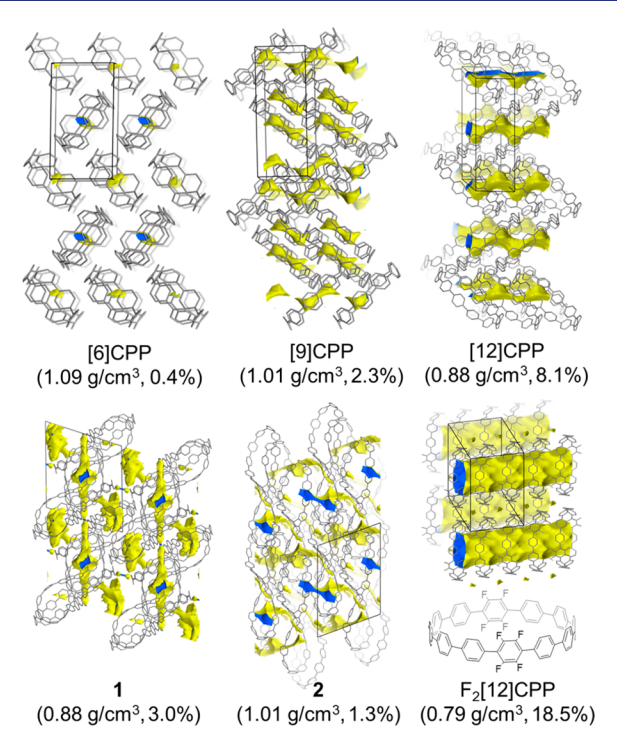


Figure 6. Solvent-accessible volume (spherical probe radius 1.8 Å, $2 \times 2 \times 2$ unit cell shown) and its ratio of the total unit cell volume for desolvated crystal structures.

partially fluorinated F₂[12]CPP was included in this study because it was recently shown to form robust supramolecular nanochannels in the solid state and therefore provides an ideal model case to explore the effect of solid-state packing. ⁵⁶ Analysis of accessible pore volume with a probe size of 1.8 Å (N₂ molecule) reveals that the herringbone-type packing of [n]CPPs is partially filling the void space of the macrocycle cavities. With increasing macrocycle size, i.e., from [6]CPP, to [9]CPP, and [12] CPP, the porosity of the crystal structures increases as indicated by (i) a decrease of the crystallographic density of the desolvated structure from 1.09, to 1.01, and 0.88 g/cm³ and (ii) concomitant increase in the accessible unit cell volume from 0.4, to 2.3, and 8.1%, respectively. More drastically, the porosity of $F_2[12]CPP$ (0.79 g/cm³, 18.5%) is enhanced owing to the formation of interconnected supramolecular nanochannels. Similar considerations for lemniscates 1 and 2 reveal a more disordered packing (1: 0.88 g/cm³, 2: 1.01 g/cm³) with significant contributions from noninterconnected interstitial space. The macrocyclic cavities of 2 are partially filled by adjacent molecules of 2 which lead to a more efficient packing with smaller accessible pore volumes of 1.3% as compared to the rather loosely packed 1 (3.0%). Hence, the intuitive correlation of macrocycle size and porosity is not observed. Instead, these results indicate that molecular geometries that prevent the typical herringbone-type packing of [n]CPPs open the possibility of complex packing effects that lead to a diverse array of bulk phases.

2.5. Small Aggregate Analyte Adsorption. Whereas predicting the bulk intermolecular packing between these compounds proved quite complex, we hypothesized that host—guest interactions between analytes and small aggregates of CPPs would be more predictive. To probe the binding affinity of the newly synthesized materials toward vapor analytes, an extensive high fundamental frequency QCM study has been

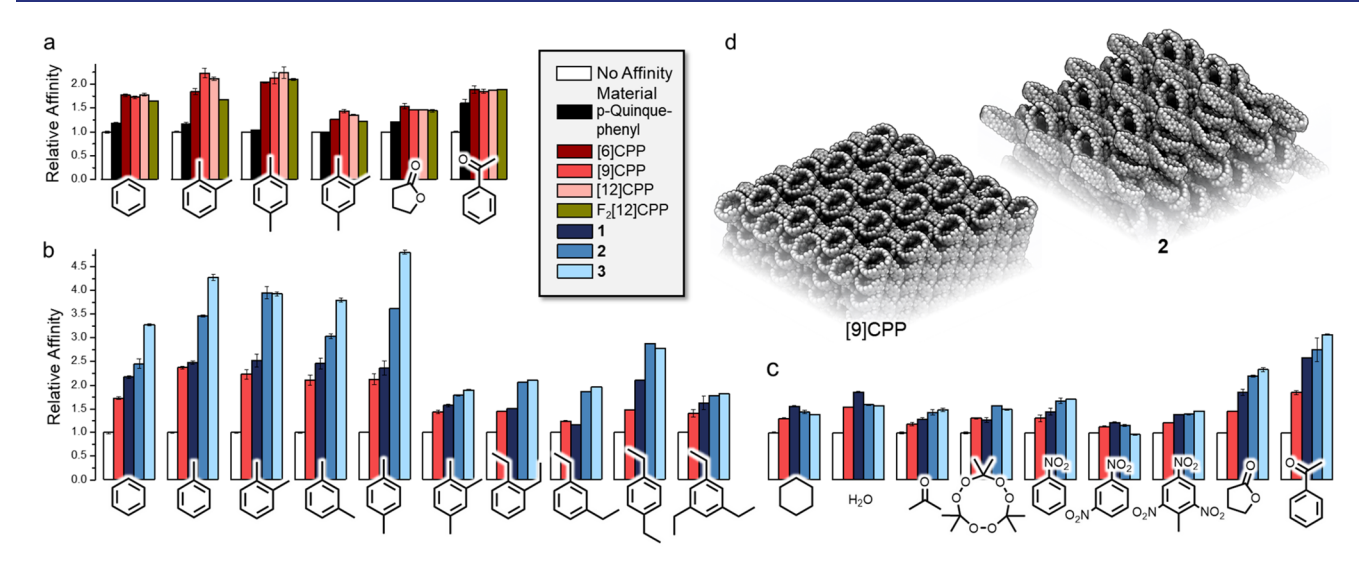


Figure 7. QCM airborne analyte sensing study of the title compounds as affinity materials relative to a passivated surface (denoted as "no affinity material"): Relative affinities of [n] CPPs (n = 6, 9, 12) and $F_2[12]$ CPP with error bars. p-Quinquephenyl was measured as a nonmacrocyclic reference to demonstrate the effect of macrocyclization (a). Comparison of the affinities of [9] CPP with lemniscates 1-3 to BTX compounds (b) and other polar and nonaromatic analytes (c). Cut out of the X-ray crystal structures of [9] CPP and 2 to exemplarily illustrate the accessibility of the nanoloop cavities and the denser packing of [9] CPP ((101) facet shown, d). For absolute data, see the Supporting Information.

performed.⁵⁷ In contrast, to N2 uptake isotherms, which are acquired at low temperatures and pressures, and probe the permanent porosity of a material, QCM measurements are performed under ambient conditions and allow inference about the host-guest interactions of supramolecular hosts in the solid state. 58-61 The benefits of this technique are multifold, ranging from small amounts of affinity materials required (in the nanogram regime), to high sensitivity (up to ppb), and the low requirements for implementation into a mobile sensing device.⁶ QCM measurements of the various host materials were performed on samples fabricated by electrospray deposition. 59,63 A detailed description of the measurement conditions and analysis is provided in the Supporting Information.⁶⁴ It is important to note that the amount of affinity material deposited (10.4 ng) corresponds to approximately 10-30 molecular layers (10-50 nm thickness) or similarly sized aggregates. 59 With the considerably larger surface to volume ratio of the samples compared to bulk measurements, this technique is amplifying the contribution from surface and close-surface cavities suitable for guest uptake. We are aware that the experimental conditions for the QCM study do not produce crystalline samples and rather represent amorphous to nanocrystalline materials. Irrespective of the long-range order, however, we postulate that the local host environment is best described by the ones observed in the crystalline bulk material, and therefore our rationale is based on the predominant interactions determined by X-ray crystallographic analysis (vide supra).

We tested various analytes from the BTX series (benzene, toluene, xylenes, mesitylene, and several diethylbenzenes), which find widespread application as rodenticides in overseas shipping containers and pose a considerable public health risk. Particularly, the differentiation of carcinogenic benzene from other BTX compounds is a challenging endeavor due to their physicochemical similarity. In addition, a range of polar aromatic compounds (nitrobenzene, trinitrotoluene (TNT), and acetophenone), polar nonaromatic compounds (water, acetone, γ -butyrolactone (GBL), and triacetone triperoxide (TATP)), and cyclohexane as nonpolar, nonaromatic compounds were tested. Some analytes included in this group have

far-reaching societal and safety implications, and hence, their detection is of current concern: GBL and acetophenone are precursors of narcotics like amphetamine and γ -hydroxybutyric acid (GHB), 60,71,72 while TNT or TATP have been used as explosives in terrorist attacks. $^{73-75}$

In an initial survey, we studied the affinity of [6]-, [9]-, [12]-, and F₂[12]CPP toward different apolar and polar analytes (Figure 7a). To explore the impact of the macrocyclic nature of the affinity materials, linear p-quinquephenyl was measured as a benchmark material. Since the phenylene-based scaffold is a common feature of all tested affinity materials, the predominant interaction with the tested analytes is based on $\pi - \pi$ stacking and $CH-\pi$ and $n \rightarrow \pi^*$ (for heteroatom-containing analytes) interactions. 76-78 For p-quinquephenyl only a small increase in affinity (approximately 10%) compared to an uncoated passivated QCM (no affinity material) was detected for all analytes except acetophenone where the affinity increased by approximately 60%. Macrocyclization has a significant positive effect as highlighted by, e.g., [12]CPP, whose affinity increases up to 222% in the case of p-xylene compared to that of pquinquephenyl. Quite surprisingly, the differences in affinity between [6]-, [9]-, and [12]CPP are rather small (average 10%) irrespective of the markedly different macrocycle sizes. DFT calculations (vide infra) suggest that the cavity size of [6] CPP the smallest derivative in this series—is not appropriate to accommodate any of the guests, and hence, analytes are most likely adsorbing to the surface of the affinity material. As the main reason for the limited cavity accessibility for the similarly performing [9]- and [12]CPP, their preferred herringbone-type packing and the resulting unfavorable uptake kinetics (e.g., selfclosing cavities)⁷⁹ can be invoked taking into account the results from X-ray analysis and gas sorption measurements (vide supra). Notably, we also find no increase in the measured affinities of F₂[12]CPP, whereas its significantly larger solvent-accessible volume (see Figure 6) paired with higher crystallinity⁵⁶ could intuitively suggest a better aptitude as affinity material. These results led us to the conclusion that nanochannel-like porous materials in general are only limitedly qualified for vapor analyte detection.

Next, we set out to explore less densely packed lemniscates 1-3. The affinities were compared to [9]CPP as a representative for the series of similarly performing [n]CPPs (Figure 7b). A general trend can be observed for the BTX analytes with rising affinities from [9]CPPs to the smallest lemniscate 1 (approximately 20%) and another drastic increase in affinity by about 70-100% for the larger derivates 2 and 3, respectively. For pxylene, compound 3 features the highest increase in affinity in the series of materials studied (480% compared to an uncoated passivated QCM) and is one of the best affinity materials for these types of analytes reported so far. 59,61 Potential size and shape selectivity of the macrocycles in the analyte uptake was studied by taking a closer look at the xylene and diethylbenzene series. As a rule of thumb, affinities are increasing toward the pderivatives (by approximately 20% and 55%) compared to their o- and m-relatives. Compound 2 represents an exception with an increased affinity toward o-xylene. The drop in the affinity owing to increased analyte size can also be seen for sterically demanding pseudocumene and 1,3,5-triethylbenzene as compared to the smaller BTX analytes. These results indicate how sensitive the lemniscates can be toward even slight structural analyte changes, with smaller, linear analytes typically showing higher affinities than their more bulky, larger derivatives. Such a size exclusion phenomenon was also reported for secondgeneration polyphenylene dendrimer host materials, which displayed a preference for smaller analytes, whereas higher generation (third and fourth) dendrimers prevailed for larger analytes. 73 Comparing the observed affinities of shape-persistent lemniscate 3 to more flexible polyphenylene dendrimers, an increase of 20% can be observed for p-xylene and even up to 70% toward m-xylene, illustrating the non-negligible role of rigidity for polyphenylene host materials.

Having unveiled the size/shape dictated affinity pattern of the BTX series, we strived to explore the impact of the analyte's aromatic subunit. To this end, we studied a variety of nonaromatic analytes-cyclohexane, water, acetone, and TATP—as well as a series of electron-deficient nitrated aromatics (Figure 7c). In these cases, we find that the preference of lemniscates 1-3 over [n]CPPs is largely suppressed as indicated by comparable and in a few cases even lower affinities. While the exact reasons for this finding are unknown, two notable exceptions are observed: GBL and acetophenone exhibit an increasing affinity toward 1-3 similar to the trend observed for the BTX analytes. Again, the favorable combination of $CO-\pi$ and $\pi-\pi$ interactions and a matching analyte size can be invoked as the key reason for the observed trend.80 A noteworthy asset is the low affinity of the tested materials toward water, which reduces interfering signals from moisture in potential sensor device applications.

Although our study corroborates the results of McKeown and co-workers⁸¹ who emphasized the importance of rigid and bulky structural elements to prevent efficient packing, it is difficult to arrive at a clear conclusion as to why lemniscates 1-3 show significantly higher affinities than [n]CPPs. It is plausible that the supramolecular arrangements of the affinity materials play a decisive role.⁸² To exemplarily illustrate the impact of the bulky spiro center in lemniscates 1-3 on the accessibility of the macrocyclic and interstitial cavities, cutouts of the crystal structures of selected affinity materials are shown in Figure 7d. For [n]CPPs (and for $F_2[12]$ CPP), a tightly packed channel-like pore morphology is preferred which minimizes void space and, in principle, only allows for analyte uptake into the channels from one dimension. In contrast, the loosely packed arrange-

ment of the lemniscates is proposedly facilitating analyte binding in that the macrocyclic binding pockets are accessible from multiple sides. Considering the nonporous nature of some of our affinity materials as evidenced by BET measurements (see Figure 4), in a classical view only surface and near-surface adsorption events should be accessible. However, a previous report on the positive effect of temperature for analyte sorption of [12] CPP suggests that these nonporous solids are not as rigid and impermeable as believed.²³ Indeed, for other macrocyclic crystalline materials, van der Waals forces have been demonstrated to enable guest transport via a cooperative diffusion mechanism with positional and/or orientational dislocation of the host 83,84—a concept which has later been described by Barbour as "porosity without pores". 85 In line with this concept, the adaptive nature of a perethylated pillar [6] arene has recently been disclosed by Cooper and co-workers. 86,87 This phenomenon was shown to enable styrene adsorption from the gas phase, despite a nonporous guest-free packing in the solid state, as evidenced by N₂ sorption experiments and X-ray crystallography. We speculate that in the present study the vapor analytes penetrate the surface of the affinity materials and subsequently accumulate in the first few layers, leading to the overall substoichiometric absolute macrocycle occupancy available from the QCM data (e.g., p-xylene/[9]CPP = 0.33, p-xylene/2 = 1.31 at 50% vapor pressure). In agreement with our findings, such a guest diffusion into the affinity material should be favored by the lemniscate series considering the weaker interhost contacts as deduced from the crystal structure (vide supra, see Figure 5b).

We noticed that our molecular host design potentially allows for affinity tuning by subtle structural manipulations such as replacement of phenylene carbons by heteroatoms. To test this hypothesis, bis(bipyridyl)-containing lemniscate 4 was compared to its similarly sized all-phenylene relative 1 (Figure 8, see

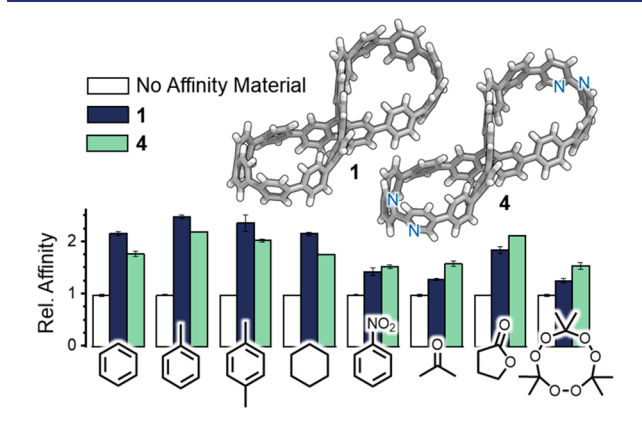


Figure 8. Comparison of the relative affinity of all-hydrocarbon lemniscate 1 and its bis(bipyridyl)-containing relative 4.

Scheme 1 for synthesis). For compound 4 the affinities toward BTX compounds are reduced by 18%. A rationale for this finding may be provided by the markedly different solid-state packing which is reminiscent of the discussed unfavorable channel like assemblies found for [n]CPP. In addition, strong phenyl—pyridyl π – π stacking and CH···N interactions result in a packing in which the macrocyclic hosts are held together, tightly presumably suppressing analyte diffusion via solid-state rearrangements (see the Supporting Information, Figure S36). S3,84 A similar effect was previously observed for [12]CPP by Itami and co-workers. Bipyridyl-embedded

[n]CPPs have been shown⁸⁸ to undergo coordination chemistry. To explore the possibility to use the bipyridyl unit as a supramolecular recognition motif, we studied a series of hydrogen-bond donors (acetone, GBL, and TATP). The affinity of 4 toward hydrogen-bond donors is generally increased by approximately 17% as compared to all-hydrocarbon 1, which we ascribe to attractive CH···N interactions. ⁸⁹ In addition, the dipolar macrocyclic cavities of bipyridyl-containing host 4 (4.42 D vs 1: 1.22 D, for details see the Supporting Information) are proposedly better suited to bind polar analytes, implicating the presence of attractive $n \rightarrow \pi^{*76,90}$ and dipole—dipole interactions ⁹¹ in the host—guest assemblies.

2.6. Theoretical Modeling. In order to better understand the experimental results, a theoretical model was developed by taking into account interaction energies, morphology, and macrocycle/analyte size effects. We commenced our investigations with a simplified model system in which the analyte/host interaction energy was correlated to the guest's solvent-accessible surface areas (SASAs) by using quantum mechanical calculations. All quantum mechanical calculations were performed with the TURBOMOLE 7.2^{92,93} or xtb 6.1⁹⁴ program packages. SASAs were predicted with UCSF Chimera. For a detailed description of our approach, which involves initial structural screening and energy calculation at the semiempirical force-field and tight-binding levels (xTB-IFF) and GFNn-xTB (pr. 98), we refer the reader to the Supporting Information. The results are represented in Figure 9a. Several

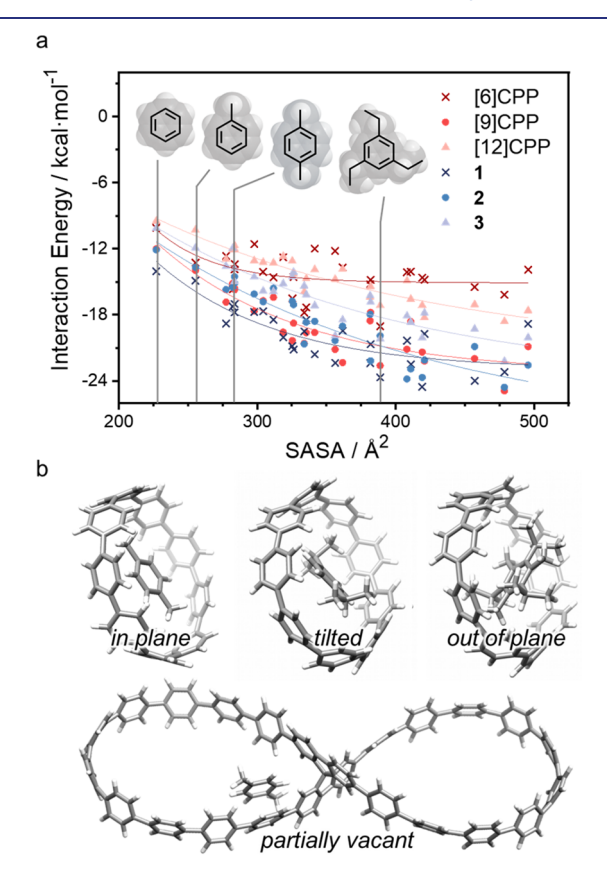


Figure 9. Plot of the relaxed DFT interaction energy on the TPSS-D3(BJ)/def2-TZVP//TPSS-D3(BJ)/def2-TZVP level of various alkyl-substituted phenylene guests with different molecular hosts vs the guest's solvent-accessible surface area (SASA, the data were fitted to the monoexponential decay function to guide the eye, a). Illustration of the different types of host/guest interaction modes (b).

trends can be observed: The predominant interaction energies—mostly dispersion and π -stacking interactions^{77,78} are found to increase with increasing SASA, i.e., with increasing amount of sp³-hybridized carbon atoms. In other words, flexible alkyl chains increase the contact surface with the host's radially oriented π -system and, hence, maximize CH- π dispersion interaction. 99 A closer inspection of the geometry-optimized host/guest assemblies reveals that the cavity of [6]CPP is too small to accommodate any of the considered guests. For the larger hosts ([9]-, [12]CPP, 1, 2, and 3), four different geometries can be observed as illustrated in Figure 9b: out-ofplane, in-plane, tilted, and partially vacant. In the case of the smallest lemniscate, 1, an out-of-plane geometry is adopted for all analytes. Medium sized hosts, [9]CPP and 2, gradually shift out-of-plane geometries for the largest analytes (e.g., 1,3,5triethyl-2,4,6-tri-iso-propylbenzene 516.8 A²) to tilted (e.g., 1,3,5-trimethylbenzene 311.7 A²) and in-plane orientation for smaller analytes (e.g., benzene 227 A²) to maximize the contact surfaces and interaction energies with the host. On the other hand, the largest macrocycles, [12]CPP and 3, are partially vacant for all probed analytes and therefore generally feature smaller interaction energies. It is worth mentioning that in this study we found no significant energetic contribution of the central V-shaped binding pockets formed by the spiro-fused fluorenes in 1–3 (see the Supporting Information, Figure S53).

While this simple model system highlights the importance of matching of host/guest sizes, it only provides an insufficient description of the experimental setup since: (i) multiple adsorption events are not considered, (ii) the available cavity space is overestimated in this molecular model neglecting selffilling cavities, and (iii) binding sites in the interstitial space, i.e., outside the macrocyclic cavities, are not considered. To account for these drawbacks, in the next step we explored a more realistic system. To this end, the affinity material was simulated using the data available from single-crystal X-ray diffraction ([9]-, [12]CPP, 1, 2, and quinquephenyl), and the void space in the large model system (four unit cells in size) was successively filled up with analyte molecules (up to a number of 50 guest molecules), applying the intermolecular force field xTB-IFF. We are aware that the use of an excerpt of the crystal structure to model the affinity material can only serve as an approximation to the experimental conditions during the QCM measurements. However, with the use of a sufficiently large model system, we strive to qualitatively simulate the range of binding pockets available in the affinity material. Briefly, our program repeatedly docks the analyte to 15 different positions in the crystal cut out, calculates single-point energies at each docking position, and chooses the one that is energetically the lowest. The interaction energies (ΔE) were calculated as the difference between the actual host-guest complex and the isolated guest and previous host—guest complex energies. Considering these time-consuming computations and analyses, four prototypical probe analytes—benzene, toluene, p-xylene, and 1,3,5-triethylbenzene—were selected from the previous experiments for this study. For reasons of better comparability with the experimental results, the average interaction energy for all 50 adsorption events was calculated and normalized to the value of pquinquephenyl.

Exemplary [9]CPP and lemniscate 2 model systems filled with *p*-xylene molecules are shown in Figure 10a, and the results of the computational study are depicted in Figure 10b. In general, the first adsorption events are energetically most favorable, and the individual host/guest interaction energies

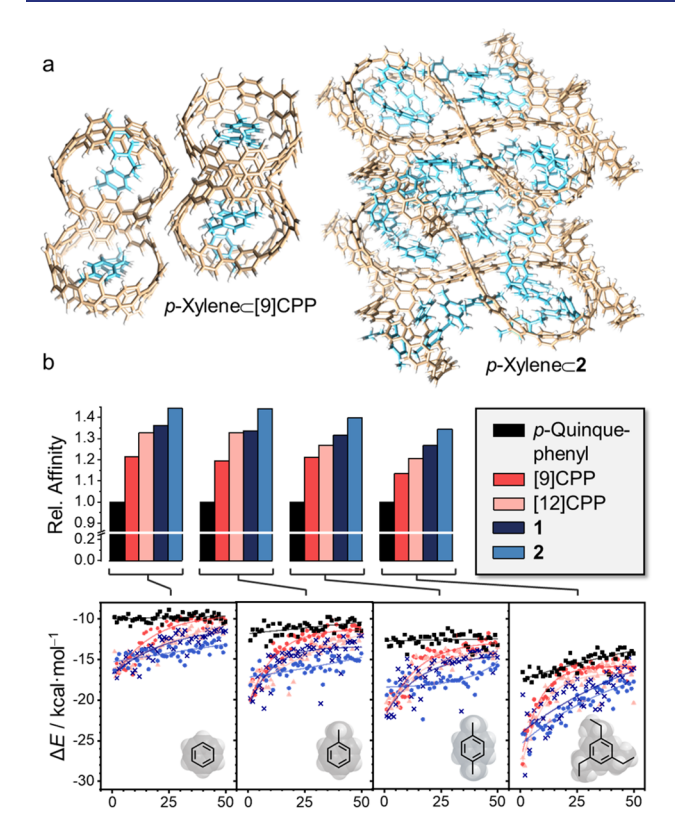


Figure 10. Theoretical model for guest uptake: partially filled [9]CPP and lemniscate **2** (analyte: *p*-xylene, a). Single-point *x*TB–IFF interaction energy (unoptimized structures) of four different guests with selected hosts vs the number of docked guest molecules (monoexponential decay curve fit to guide the eye). Relative affinities were estimated by calculating the mean interaction energy over all 50 adsorption events and normalizing to *p*-quinquephenyl (b).

gradually decrease with the number of guests added. The pquinquephenyl trace indicates the saturation limit, as its dense crystal packing 101 only allows for surface adsorption owing to the complete absence of cavities. With increasing alkyl-chain content of the guests, i.e., from benzene to 1,3,5-triethylbenzene, the curve of p-quinquephenyl shows an increasing slope which we ascribe to stronger host/guest CH $-\pi$ dispersion interactions in agreement with the findings from the molecular model systems (see Figure 9a). The first adsorption events for a specific analyte are energetically alike for all hosts (except pquinquephenyl) in the crystal model system, in contrast to the energetic differences determined for the molecular system. This finding indicates the presence of energetically more favorable interstitial binding sites in addition to the macrocyclic cavities. For later adsorptions, the larger hosts outperform their smaller relatives by providing a larger number of energetically more favorable binding sites. Consequently, the saturation observed for all affinity materials is most pronounced for the smaller hosts in the respective series, [9]CPP and 1. Here, suitably large binding sites are more rapidly filled up as indicated by a steeper slope, which can be regarded as another key reason for the better affinities of the larger macrocycles. In other words, lemniscal hosts 1 and 2 show higher interaction energies over a wider number of adsorption events as compared to the [n]CPP series. Based on this model the more disordered packing of the lemniscate family is playing a crucial role for the experimentally observed high affinities in the QCM measurements. We would like to note that, in the theoretical discussion, dynamic guest

uptake processes such as a cooperative diffusion mechanism are not considered. While this shortcoming may serve as an impetus for future computational studies, the good qualitative agreement of our results with the affinity trends observed in QCM study suggest that the developed simplified theoretical model can be used for the computer-assisted design of high affinity materials.

CONCLUSION

In conclusion, the bottom-up synthesis of atomically defined and solution-processable lemniscal nanocarbons with shapepersistent cavities is presented. Our simple molecular design, using phenylenes as the sole building blocks, permitted the manipulation of the solid-state structure of the parent [n] CPPs without considerably changing the size and nature of the built-in cavity. This manipulation allowed insight into the intricate interplay of the molecular and solid-state structure that dictates porosity and analyte uptake capabilities. We find that smallmolecule sorption in intrinsically porous macrocyclic nanocarbons can be remarkably disparate when going from bulk materials to small aggregates, and thus, correlations between measurements need to be treated with caution. Conclusions drawn from low or nonexisting surface areas in BET measurements, for instance, may mistakenly eliminate potential candidates for analyte sensing applications. Paradigmatically, in QCM-based sensing experiments where our novel lemniscates served as host material, a remarkable increase of the affinities toward vapor analytes of up to 480% compared to an uncoated passivated QCM was observed regardless of the bulk surface areas. In contrast, hoop-shaped [n]CPPs were generally found unsuitable for analyte uptake despite similar cavity sizes. Our study indicates that: (i) less ordered, more loosely packed macrocycles provide more abundant and accessible void space, and thus, host-host interactions are pivotal for analyte uptake. In other words, the tight herringbone-type packing of CPPs is unfavorable in that it minimizes interstitial and macrocyclic void space and hampers structural rearrangement of the macrocycles in the solid state upon analyte contact. (ii) It is possible to finetune the analyte selectivity by heteroatom substitution in the hosts. Replacement of phenyl by pyridyl rings, for instance, leads to higher affinities for more polar and CH-acidic analytes. The quantum chemistry treatment revealed that a molecular model is not suitable to quantitatively describe the substrate affinity, due to the decisive influence of the crystal structure arrangement. Consideration of a crystal cut-out of four unit cells (with about 400-3100 atoms) was sufficient for a semiquantitative description of the experimentally observed affinity values. The theoretical modeling demonstrated that (iii) the larger the guest molecules (and thus the contact surface with the host), the stronger the CH $-\pi$ dispersive interactions. (iv) Subsurface adsorption sites provide an important energetic contribution to the observed affinities in cases where tight packing is prevented by suitable molecular design, and the built-in cavity is large enough to enable analyte accessibility. (vi) The more interstitial void space that is in the crystal structure, the more analyte that can be taken up. The favorable combination of (i)-(vi) offers a rationale for the experimentally observed affinities. With this study situated at the interface of molecular entities, small aggregates, and materials, we provide insight into a current challenge for the fabrication of functional porous materials from discrete organic molecules—the transition from molecular to materials properties. It is important to note, though, that the solid-state arrangement as a decisive factor for porosity may not be obvious from the molecular building blocks in isolation, and thus, further research into novel discrete carbon-rich architectures as specialized porous materials is required.

ASSOCIATED CONTENT

Supporting Information

The Supporting Information is available free of charge at https://pubs.acs.org/doi/10.1021/jacs.0c01117.

Experimental Procedures (PDF)

Crystallographic data for 1 (CIF)

Crystallographic data for 2 (CIF)

Crystallographic data for 4 (CIF)

AUTHOR INFORMATION

Corresponding Authors

Ramesh Jasti — Department of Chemistry & Biochemistry and Material Science Institute and Knight Campus for Accelerating Scientific Impact, University of Oregon, Eugene, Oregon 97403, United States; orcid.org/0000-0002-8606-6339; Email: rjasti@uoregon.edu

Tobias A. Schaub — Department of Chemistry & Biochemistry and Material Science Institute and Knight Campus for Accelerating Scientific Impact, University of Oregon, Eugene, Oregon 97403, United States; Institute of Organic Chemistry, Ruprecht-Karls University of Heidelberg, Heidelberg 69120, Germany; ⊕ orcid.org/0000-0003-1208-1824; Email: tschaub@uoregon.edu

Authors

Ephraim A. Prantl – Department of Organic Chemistry, Johannes Gutenberg-University Mainz, Mainz 55128, Germany

Julia Kohn — Mulliken Center for Theoretical Chemistry, University Bonn, Bonn 53115, Germany

Markus Bursch — Mulliken Center for Theoretical Chemistry, University Bonn, Bonn 53115, Germany; ⊚ orcid.org/0000-0001-6711-5804

Checkers R. Marshall – Department of Chemistry & Biochemistry and Material Science Institute and Knight Campus for Accelerating Scientific Impact, University of Oregon, Eugene, Oregon 97403, United States

Erik J. Leonhardt — Department of Chemistry & Biochemistry and Material Science Institute and Knight Campus for Accelerating Scientific Impact, University of Oregon, Eugene, Oregon 97403, United States; ◎ orcid.org/0000-0002-5380-2328

Terri C. Lovell – Department of Chemistry & Biochemistry and Material Science Institute and Knight Campus for Accelerating Scientific Impact, University of Oregon, Eugene, Oregon 97403, United States

Lev N. Zakharov – Department of Chemistry & Biochemistry and Material Science Institute, University of Oregon, Eugene, Oregon 97403, United States

Carl K. Brozek – Department of Chemistry & Biochemistry and Material Science Institute, University of Oregon, Eugene, Oregon 97403, United States; orcid.org/0000-0002-8014-7904

Siegfried R. Waldvogel — Department of Organic Chemistry, Johannes Gutenberg-University Mainz, Mainz 55128, Germany; orcid.org/0000-0002-7949-9638

Stefan Grimme – Mulliken Center for Theoretical Chemistry, University Bonn, Bonn 53115, Germany; ⊚ orcid.org/0000-0002-5844-4371

Complete contact information is available at:

https://pubs.acs.org/10.1021/jacs.0c01117

Author Contributions

The manuscript was written through contributions of all authors.

Notes

The authors declare no competing financial interest.

ACKNOWLEDGMENTS

Funding by Deutsche Forschungsgemeinschaft is gratefully acknowledged (DFG Postdoctoral Fellowship SCHA 2061/1-1 and Return Scholarship SCHA 2061/1-2 to T.S and Leibniz prize to S.G.). R.J. acknowledges funding from the National Science Foundation (CHE-1800586).

■ REFERENCES

- (1) Stein, A.; Wang, Z.; Fierke, M. A. Functionalization of Porous Carbon Materials with Designed Pore Architecture. *Adv. Mater.* **2009**, 21, 265–293.
- (2) Lü, J.; Cao, R. Porous Organic Molecular Frameworks with Extrinsic Porosity: A Platform for Carbon Storage and Separation. *Angew. Chem., Int. Ed.* **2016**, *55*, 9474–9480.
- (3) Yuan, S.; Li, X.; Zhu, J.; Zhang, G.; van Puyvelde, P.; van der Bruggen, B. Covalent Organic Frameworks for Membrane Separation. *Chem. Soc. Rev.* **2019**, *48*, 2665–2681.
- (4) Rodríguez-Reinoso, F. The Role of Carbon Materials in Heterogeneous Catalysis. *Carbon* **1998**, *36*, 159–175.
- (5) Cao, Y.; Mao, S.; Li, M.; Chen, Y.; Wang, Y. Metal/Porous Carbon Composites for Heterogeneous Catalysis: Old Catalysts with Improved Performance Promoted by N-Doping. ACS Catal. 2017, 7, 8090—8112.
- (6) White, R. J.; Budarin, V.; Luque, R.; Clark, J. H.; Macquarrie, D. J. Tuneable Porous Carbonaceous Materials From Renewable Resources. *Chem. Soc. Rev.* **2009**, *38*, 3401–3418.
- (7) Zhai, Y.; Dou, Y.; Zhao, D.; Fulvio, P. F.; Mayes, R. T.; Dai, S. Carbon Materials for Chemical Capacitive Energy Storage. *Adv. Mater.* **2011**, 23, 4828–4850.
- (8) Forse, A. C.; Merlet, C.; Griffin, J. M.; Grey, C. P. New Perspectives on the Charging Mechanisms of Supercapacitors. *J. Am. Chem. Soc.* **2016**, *138*, 5731–5744.
- (9) Candelaria, S. L.; Shao, Y.; Zhou, W.; Li, X.; Xiao, J.; Zhang, J.-G.; Wang, Y.; Liu, J.; Li, J.; Cao, G. Nanostructured Carbon for Energy Storage and Conversion. *Nano Energy* **2012**, *1*, 195–220.
- (10) Gu, W.; Yushin, G. Review of Nanostructured Carbon Materials for Electrochemical Capacitor Applications: Advantages and Limitations of Activated Carbon, Carbide-Derived Carbon, Zeolite-Templated Carbon, Carbon Aerogels, Carbon Nanotubes, Onion-Like Carbon, and Graphene. WIREs Energy Environ. 2014, 3, 424–473.
- (11) Das, S.; Heasman, P.; Ben, T.; Qiu, S. Porous Organic Materials: Strategic Design and Structure-Function Correlation. *Chem. Rev.* **2017**, 117, 1515–1563.
- (12) Li, J.-R.; Sculley, J.; Zhou, H.-C. Metal-Organic Frameworks for Separations. *Chem. Rev.* **2012**, *112*, 869–932.
- (13) Wang, K.-X.; Li, X.-H.; Chen, J.-S. Surface and Interface Engineering of Electrode Materials for Lithium-Ion Batteries. *Adv. Mater.* **2015**, 27, 527–545.
- (14) Park, H. B.; Jung, C. H.; Lee, Y. M.; Hill, A. J.; Pas, S. J.; Mudie, S. T.; van Wagner, E.; Freeman, B. D.; Cookson, D. J. Polymers with Cavities Tuned for Fast Selective Transport of Small Molecules and Ions. *Science* **2007**, *318*, 254–258.
- (15) Lu, A.-H.; Hao, G.-P.; Sun, Q.; Zhang, X.-Q.; Li, W.-C. Chemical Synthesis of Carbon Materials With Intriguing Nanostructure and Morphology. *Macromol. Chem. Phys.* **2012**, *213*, 1107–1131.
- (16) Zou, X.; Ren, H.; Zhu, G. Topology-Directed Design of Porous Organic Frameworks and Their Advanced Applications. *Chem. Commun.* **2013**, *49*, 3925–3936.
- (17) Liang, C.; Li, Z.; Dai, S. Mesoporous Carbon Materials: Synthesis and Modification. *Angew. Chem., Int. Ed.* **2008**, 47, 3696–3717.

- (18) Ben, T.; Qiu, S. Porous Aromatic Frameworks: Synthesis, Structure and Functions. *CrystEngComm* **2013**, *15*, 17–26.
- (19) Tian, J.; Thallapally, P. K.; McGrail, B. P. Porous Organic Molecular Materials. *CrystEngComm* **2012**, *14*, 1909–1919.
- (20) Holst, J. R.; Trewin, A.; Cooper, A. I. Porous Organic Molecules. *Nat. Chem.* **2010**, *2*, 915–920.
- (21) Evans, J. D.; Jelfs, K. E.; Day, G. M.; Doonan, C. J. Application of Computational Methods to the Design and Characterisation of Porous Molecular Materials. *Chem. Soc. Rev.* **2017**, *46*, 3286–3301.
- (22) Zhou, Y.; Jie, K.; Zhao, R.; Huang, F. Supramolecular-Macrocycle-Based Crystalline Organic Materials. *Adv. Mater.* **2019**, 1904824.
- (23) Sakamoto, H.; Fujimori, T.; Li, X.; Kaneko, K.; Kan, K.; Ozaki, N.; Hijikata, Y.; Irle, S.; Itami, K. Cycloparaphenylene as a Molecular Porous Carbon Solid with Uniform Pores Exhibiting Adsorption-Induced Softness. *Chem. Sci.* **2016**, *7*, 4204–4210.
- (24) Lin, J. B.; Darzi, E. R.; Jasti, R.; Yavuz, I.; Houk, K. N. Solid-State Order and Charge Mobility in [5]- to [12] Cycloparaphenylenes. *J. Am. Chem. Soc.* **2019**, *141*, 952–960.
- (25) [6] CPP is the only exception in that a second polymorph exists. See: Fukushima, T.; Sakamoto, H.; Tanaka, K.; Hijikata, Y.; Irle, S.; Itami, K. Polymorphism of [6] Cycloparaphenylene for Packing Structure-dependent Host-Guest Interaction. *Chem. Lett.* **2017**, *46*, 855–857.
- (26) Segawa, Y.; Senel, P.; Matsuura, S.; Omachi, H.; Itami, K. [9] Cycloparaphenylene: Nickel-Mediated Synthesis and Crystal Structure. *Chem. Lett.* **2011**, *40*, 423–425.
- (27) Saenger, W.; Steiner, T. Cyclodextrin Inclusion Complexes: Host–Guest Interactions and Hydrogen-Bonding Networks. *Acta Crystallogr., Sect. A: Found. Crystallogr.* 1998, 54, 798–805.
- (28) Saenger, W. Nature and Size of Included Guest Molecule Determines Architecture of Crystalline Cyclodextrin Host Matrix. *Isr. J. Chem.* **1985**, 25, 43–50.
- (29) Harata, K. Crystallographic Study of Cyclodextrins and Their Inclusion Complexes. In *Cyclodextrins and their complexes: Chemistry, analytical methods, applications*; Dodziuk, H., Ed.; Wiley-VCH: Weinheim, 2006; pp 147–198.
- (30) Steiner, T.; Koellner, G. Crystalline.beta.-Cyclodextrin Hydrate at Various Humidities: Fast, Continuous, and Reversible Dehydration Studied by X-ray Diffraction. *J. Am. Chem. Soc.* **1994**, *116*, 5122–5128.
- (31) Bardelang, D.; Udachin, K. A.; Leek, D. M.; Margeson, J. C.; Chan, G.; Ratcliffe, C. I.; Ripmeester, J. A. Cucurbit[n]urils (n = 5-8): A Comprehensive Solid State Study. *Cryst. Growth Des.* **2011**, *11*, 5598-5614.
- (32) Hwang, I.; Jeon, W. S.; Kim, H.-J.; Kim, D.; Kim, H.; Selvapalam, N.; Fujita, N.; Shinkai, S.; Kim, K. Cucurbit7uril: A Simple Macrocyclic, pH-triggered Hydrogelator Exhibiting Guest-induced Stimuli-responsive Behavior. *Angew. Chem., Int. Ed.* **2007**, *46*, 210–213.
- (33) Sprafke, J. K.; Kondratuk, D. V.; Wykes, M.; Thompson, A. L.; Hoffmann, M.; Drevinskas, R.; Chen, W.-H.; Yong, C. K.; Kärnbratt, J.; Bullock, J. E.; Malfois, M.; Wasielewski, M. R.; Albinsson, B.; Herz, L. M.; Zigmantas, D.; Beljonne, D.; Anderson, H. L. Belt-Shaped π-Systems: Relating Geometry to Electronic Structure in a Six-Porphyrin Nanoring. *J. Am. Chem. Soc.* **2011**, *133*, 17262–17273.
- (34) Jasti, R.; Bhattacharjee, J.; Neaton, J. B.; Bertozzi, C. R. Synthesis, Characterization, and Theory of [9]-, [12]-, and [18]-Cycloparaphenylene: Carbon Nanohoop Structures. *J. Am. Chem. Soc.* **2008**, *130*, 17646–17647.
- (35) Matsui, K.; Segawa, Y.; Itami, K. All-Benzene Carbon Nanocages: Size-Selective Synthesis, Photophysical Properties, and Crystal Structure. *J. Am. Chem. Soc.* **2014**, *136*, 16452–16458.
- (36) Xu, W.; Yang, X.-D.; Fan, X.-B.; Wang, X.; Tung, C.-H.; Wu, L.-Z.; Cong, H. Synthesis and Characterization of a Pentiptycene-Derived Dual Oligoparaphenylene Nanohoop. *Angew. Chem., Int. Ed.* **2019**, *58*, 3943–3947.
- (37) Huang, Z.-A.; Chen, C.; Yang, X.-D.; Fan, X.-B.; Zhou, W.; Tung, C.-H.; Wu, L.-Z.; Cong, H. Synthesis of Oligoparaphenylene-Derived Nanohoops Employing an Anthracene Photodimerization-Cycloreversion Strategy. J. Am. Chem. Soc. 2016, 138, 11144–11147.

- (38) During the preparation of this manuscript, a similar lemniscal architecture was published: Senthilkumar, K.; Kondratowicz, M.; Lis, T.; Chmielewski, P. J.; Cybinska, J.; Zafra, J. L.; Casado, J.; Vives, T.; Crassous, J.; Favereau, L.; Stępień, M. Lemniscular [16]-Cycloparaphenylene: A Radially Conjugated Figure-Eight Aromatic Molecule. J. Am. Chem. Soc. 2019, 141, 7421–7427.
- (39) Bachrach, S. M. Cycloparaphenylene Lemniscates and Trefoils. *J. Org. Chem.* **2020**, *85*, 674–681.
- (40) Grimme, S.; Antony, J.; Ehrlich, S.; Krieg, H. A Consistent and Accurate Ab Initio Parametrization of Density Functional Dispersion Correction (DFT-D) for the 94 Elements H-Pu. *J. Chem. Phys.* **2010**, 132, 154104.
- (41) Johnson, E. R.; Becke, A. D. A Post-Hartree-Fock Model of Intermolecular Interactions. *J. Chem. Phys.* **2005**, *123*, 024101.
- (42) Becke, A. D.; Johnson, E. R. A Density-Functional Model of the Dispersion Interaction. *J. Chem. Phys.* **2005**, *123*, 154101.
- (43) Tao, J.; Perdew, J. P.; Staroverov, V. N.; Scuseria, G. E. Climbing the Density Functional Ladder: Nonempirical Meta-Generalized Gradient Approximation Designed for Molecules and Solids. *Phys. Rev. Lett.* **2003**, *91*, 146401.
- (44) Weigend, F.; Ahlrichs, R. Balanced Basis Sets of Split Valence, Triple Zeta Valence and Quadruple Zeta Valence Quality for H to Rn: Design and Assessment of Accuracy. *Phys. Chem. Chem. Phys.* **2005**, *7*, 3297–3305.
- (45) Darzi, E. R.; Jasti, R. The Dynamic, Size-Dependent Properties of [5]-[12]Cycloparaphenylenes. *Chem. Soc. Rev.* **2015**, *44*, 6401–6410.
- (46) Segawa, Y.; Omachi, H.; Itami, K. Theoretical Studies on the Structures and Strain Energies of Cycloparaphenylenes. *Org. Lett.* **2010**, 12, 2262–2265.
- (47) Patel, V. K.; Kayahara, E.; Yamago, S. Practical Synthesis of [n]Cycloparaphenylenes (n = 5, 7–12) by H2SnCl4-Mediated Aromatization of 1,4-Dihydroxycyclo-2,5-diene Precursors. *Chem. Eur. J.* **2015**, *21*, 5742–5749.
- (48) Darzi, E. R.; Sisto, T.; Jasti, R. Selective Syntheses of [7]-[12]Cycloparaphenylenes Using Orthogonal Suzuki-Miyaura Cross-Coupling Reactions. *J. Org. Chem.* **2012**, *77*, 6624–6628.
- (49) Adamska, L.; Nayyar, I.; Chen, H.; Swan, A. K.; Oldani, N.; Fernandez-Alberti, S.; Golder, M. R.; Jasti, R.; Doorn, S. K.; Tretiak, S. Self-Trapping of Excitons, Violation of Condon Approximation, and Efficient Fluorescence in Conjugated Cycloparaphenylenes. *Nano Lett.* **2014**, *14*, 6539–6546.
- (50) Iwamoto, T.; Watanabe, Y.; Sakamoto, Y.; Suzuki, T.; Yamago, S. Selective and random syntheses of ncycloparaphenylenes (n = 8–13) and size dependence of their electronic properties. *J. Am. Chem. Soc.* **2011**, *133*, 8354–8361.
- (51) Evans, P. J.; Darzi, E. R.; Jasti, R. Efficient room-temperature synthesis of a highly strained carbon nanohoop fragment of buckminsterfullerene. *Nat. Chem.* **2014**, *6*, 404–408.
- (52) Li, P.; Sisto, T. J.; Darzi, E. R.; Jasti, R. The effects of cyclic conjugation and bending on the optoelectronic properties of paraphenylenes. *Org. Lett.* **2014**, *16*, 182–185.
- (53) Werner, A.; Michels, M.; Zander, L.; Lex, J.; Vogel, E. Figure Eight" Cyclooctapyrroles: Enantiomeric Separation and Determination of the Absolute Configuration of a Binuclear Metal Complex. *Angew. Chem., Int. Ed.* **1999**, *38*, 3650–3653.
- (54) Xia, J.; Jasti, R. Synthesis, Characterization, and Crystal Structure of [6] Cycloparaphenylene. *Angew. Chem., Int. Ed.* **2012**, *51*, 2474–2476.
- (55) Segawa, Y.; Miyamoto, S.; Omachi, H.; Matsuura, S.; Senel, P.; Sasamori, T.; Tokitoh, N.; Itami, K. Concise Synthesis and Crystal Structure of [12] Cycloparaphenylene. *Angew. Chem., Int. Ed.* **2011**, *50*, 3244–3248.
- (56) van Raden, J. M.; Leonhardt, E. J.; Zakharov, L. N.; Pérez-Guardiola, A.; Pérez-Jiménez, Á. J.; Marshall, C. R.; Brozek, C. K.; Sancho-García, J. C.; Jasti, R. Precision Nanotube Mimics via Self-Assembly of Programmed Carbon Nanohoops. *J. Org. Chem.* **2020**, *85*, 129–141.
- (57) This technique has proved advantageous to determine the binding affinity of small molecular affinity materials towards vapor

- analytes under ambient conditions. For selected examples, see refs 58-61.
- (58) Prantl, E.; Kohl, B.; Ryvlin, D.; Biegger, P.; Wadepohl, H.; Rominger, F.; Bunz, U. H. F.; Mastalerz, M.; Waldvogel, S. R. Microporous Triptycene-Based Affinity Materials on Quartz Crystal Microbalances for Tracing of Illicit Compounds. *ChemPlusChem* **2019**, 84, 1239.
- (59) Brutschy, M.; Schneider, M. W.; Mastalerz, M.; Waldvogel, S. R. Porous Organic Cage Compounds as Highly Potent Affinity Materials for Sensing by Quartz Crystal Microbalances. *Adv. Mater.* **2012**, *24*, 6049–6052.
- (60) Brutschy, M.; Schneider, M. W.; Mastalerz, M.; Waldvogel, S. R. Direct Gravimetric Sensing of GBL by a Molecular Recognition Process in Organic Cage Compounds. *Chem. Commun.* **2013**, *49*, 8398–8400.
- (61) Pyka, I.; Ryvlin, D.; Waldvogel, S. R. Application of Rigidity-Controlled Supramolecular Affinity Materials for the Gravimetric Detection of Hazardous and Illicit Compounds. *ChemPlusChem* **2016**, *81*, 926–929.
- (62) Wessels, A.; Klöckner, B.; Siering, C.; Waldvogel, S. R. Practical Strategies for Stable Operation of HFF-QCM in Continuous Air Flow. *Sensors* **2013**, *13*, 12012–12029.
- (63) Fenn, J. B. Electrospray Wings for Molecular Elephants (Nobel Lecture). *Angew. Chem., Int. Ed.* **2003**, 42, 3871–3894.
- (64) Brutschy, M.; Lubczyk, D.; Müllen, K.; Waldvogel, S. R. Surface Pretreatment Boosts the Performance of Supramolecular Affinity Materials on Quartz Crystal Microbalances for Sensor Applications. *Anal. Chem.* **2013**, *85*, 10526–10530.
- (65) Baur, X.; Ollesch, T.; Poschadel, B.; Budnik, L. T.; Finger, S.; Matz, G. Begasungsmittelrückstände und toxische Industriechemikalien in Import-Containern. Zentralbl. Arbeitsmed., Arbeitsschutz Ergon. 2007, 57, 89–104.
- (66) Zampolli, S.; Elmi, I.; Mancarella, F.; Betti, P.; Dalcanale, E.; Cardinali, G. C.; Severi, M. Real-Time Monitoring of sub-ppb Concentrations of Aromatic Volatiles with a MEMS-Enabled Miniaturized Gas-Chromatograph. Sens. Actuators, B 2009, 141, 322–328.
- (67) Clément, P.; Korom, S.; Struzzi, C.; Parra, E. J.; Bittencourt, C.; Ballester, P.; Llobet, E. Deep Cavitand Self-Assembled on Au NPs-MWCNT as Highly Sensitive Benzene Sensing Interface. *Adv. Funct. Mater.* **2015**, 25, 4011–4020.
- (68) Bertani, F.; Riboni, N.; Bianchi, F.; Brancatelli, G.; Sterner, E. S.; Pinalli, R.; Geremia, S.; Swager, T. M.; Dalcanale, E. Triptycene-Roofed Quinoxaline Cavitands for the Supramolecular Detection of BTEX in Air. *Chem. Eur. J.* **2016**, *22*, 3312–3319.
- (69) Zampolli, S.; Betti, P.; Elmi, I.; Dalcanale, E. A Supramolecular Approach to sub-ppb Aromatic VOC Detection in Air. *Chem. Commun.* **2007**, 2790–2792.
- (70) Dickert, F. L.; Lieberzeit, P.; Miarecka, S. G.; Mann, K. J.; Hayden, O.; Palfinger, C. Synthetic Receptors for Chemical Sensors Subnano- and Micrometre Patterning by Imprinting Techniques. *Biosens. Bioelectron.* **2004**, *20*, 1040–1044.
- (71) Gimeno, P.; Besacier, F.; Bottex, M.; Dujourdy, L.; Chaudron-Thozet, H. A Study of Impurities in Intermediates and 3,4-Methylenedioxymethamphetamine (MDMA) Samples Produced via reductive amination routes. *Forensic Sci. Int.* **2005**, *155*, 141–157.
- (72) Trachsel, D. Psychedelische Chemie: Aspekte psychoaktiver Moleküle, 4th ed.; Nachtschatten-Verl.: Solothurn, 2011.
- (73) Gardner, J. W.; Yinon, J. Electronic Noses & Sensors for the Detection of Explosives; NATO Science Series II 159; Springer Science: Dordrecht, 2004.
- (74) Detection of Liquid Explosives and Flammable Agents in Connection with Terrorism; Schubert, H., Kuznetsov, A., Eds.; NATO Science for Peace and Security Series B: Physics and Biophysics; Springer Netherlands: Dordrecht, 2008.
- (75) Oxley, J. C. What's Special About Liquid Explosives? In *Detection of Liquid Explosives and Flammable Agents in Connection with Terrorism*; Schubert, H., Kuznetsov, A., Eds.; NATO Science for Peace and Security Series B: Physics and Biophysics; Springer Netherlands: Dordrecht, 2008; pp 27–38.

- (76) Newberry, R. W.; Raines, R. T. The $n \rightarrow \pi^*$ Interaction. *Acc. Chem. Res.* **2017**, *50*, 1838–1846.
- (77) Hunter, C. A.; Sanders, J. K. M. The Nature of π - π Interactions. *J. Am. Chem. Soc.* **1990**, *112*, 5525–5534.
- (78) Grimme, S. Do Special Noncovalent π - π Stacking Interactions Really Exist? *Angew. Chem., Int. Ed.* **2008**, *47*, 3430–3434.
- (79) Brutschy, M.; Stangenberg, R.; Beer, C.; Lubczyk, D.; Baumgarten, M.; Müllen, K.; Waldvogel, S. R. The Generation Effect: Cavity Accessibility in Dense-Shell Polyphenylene Dendrimers. *ChemPlusChem* **2015**, *80*, 54–56.
- (80) Li, P.; Vik, E. C.; Maier, J. M.; Karki, I.; Strickland, S. M. S.; Umana, J. M.; Smith, M. D.; Pellechia, P. J.; Shimizu, K. D. Electrostatically Driven CO- π Aromatic Interactions. *J. Am. Chem. Soc.* **2019**, *141*, 12513–12517.
- (81) Abbott, L. J.; McKeown, N. B.; Colina, C. M. Design Principles for Microporous Organic Solids From Predictive Computational Screening. *J. Mater. Chem. A* **2013**, *1*, 11950–11960.
- (82) For the discussion we leave aside differences in the shape of the macrocyclic cavities (round vs drop shaped), which were shown to not significantly contribute to the affinities (see the SI, Figure S52).
- (83) Thallapally, P. K.; Lloyd, G. O.; Atwood, J. L.; Barbour, L. J. Diffusion of Water in a Nonporous Hydrophobic Crystal. *Angew. Chem., Int. Ed.* **2005**, *44*, 3848–3851.
- (84) Atwood, J. L.; Barbour, L. J.; Jerga, A.; Schottel, B. L. Guest Transport in a Nonporous Organic Solid via Dynamic van der Waals Cooperativity. *Science* **2002**, *298*, 1000–1002.
- (85) Barbour, L. J. Crystal Porosity and the Burden of Proof. Chem. Commun. 2006, 1163–1168.
- (86) Jie, K.; Liu, M.; Zhou, Y.; Little, M. A.; Bonakala, S.; Chong, S. Y.; Stephenson, A.; Chen, L.; Huang, F.; Cooper, A. I. Styrene Purification by Guest-Induced Restructuring of Pillar6arene. *J. Am. Chem. Soc.* **2017**, 139, 2908–2911.
- (87) For a review of nonporous adaptive crystals, see: Jie, K.; Zhou, Y.; Li, E.; Huang, F. Nonporous Adaptive Crystals of Pillararenes. *Acc. Chem. Res.* **2018**, *51*, 2064–2072.
- (88) van Raden, J. M.; Louie, S.; Zakharov, L. N.; Jasti, R. 2,2′-Bipyridyl-Embedded Cycloparaphenylenes as a General Strategy To Investigate Nanohoop-Based Coordination Complexes. *J. Am. Chem. Soc.* 2017, 139, 2936–2939.
- (89) Gilday, L. C.; Robinson, S. W.; Barendt, T. A.; Langton, M. J.; Mullaney, B. R.; Beer, P. D. Halogen Bonding in Supramolecular Chemistry. *Chem. Rev.* **2015**, *115*, 7118–7195.
- (90) Singh, S. K.; Das, A. The $n \to \pi^*$ Interaction: A Rapidly Emerging Non-Covalent Interaction. *Phys. Chem. Chem. Phys.* **2015**, *17*, 9596–9612.
- (91) Della Sala, P.; Talotta, C.; Caruso, T.; De Rosa, M.; Soriente, A.; Neri, P.; Gaeta, C. Tuning Cycloparaphenylene Host Properties by Chemical Modification. *J. Org. Chem.* **2017**, *82*, 9885–9889.
- (92) Furche, F.; Ahlrichs, R.; Hättig, C.; Klopper, W.; Sierka, M.; Weigend, F. Turbomole. *Wiley Interdiscip. Rev.: Comput. Mol. Sci.* **2014**, 4, 91–100.
- (93) Ahlrichs, R.; Armbruster, M. K.; Bachorz, R. A.; Bär, M.; Baron, H.; Bauernschmitt, R.; Bischoff, F. A.; Böcker, S.; Burow, A. M.; Crawford, N.; Deglmann, P.; Sala, F. D.; Diedenhofen, M.; Ehrig, M.; Eichkorn, K.; Elliott, S.; Friese, D.; Furche, F.; Glöß, A.; Graf, N.; Grajciar, L.; Haase, F.; Häser, M.; Hättig, C.; Hellweg, A.; Helmich, B.; Höfener, S.; Horn, H.; Huber, C.; Huniar, U.; Kattannek, M.; Klopper, W.; Köhn, A.; Kölmel, C.; Kollwitz, M.; Kühn, M.; May, K.; Nava, P.; Ochsenfeld, C.; Öhm, H.; Pabst, M.; Patzelt, H.; Rappoport, D.; Rubner, O.; Schäfer, A.; Schmitz, G.; Schneider, U.; Sierka, M.; Tew, D. P.; Treutler, O.; Unterreiner, B.; von Arnim, M.; Weigend, F.; Weis, P.; Weiss, H.; Winter, N. *TURBOMOLE 7.2*, Universität Karlsruhe, 2017. See also: http://www.turbomole.com.
- (94) Semiempirical extended tight-binding program package xtb, version 6.1; https://github.com/grimme-lab/xtb. Accessed: April 21, 2020.
- (95) Pettersen, E. F.; Goddard, T. D.; Huang, C. C.; Couch, G. S.; Greenblatt, D. M.; Meng, E. C.; Ferrin, T. E. UCSF Chimera A Visualization System for Exploratory Research and Analysis. *J. Comput. Chem.* **2004**, *25*, 1605–1612.

- (96) Grimme, S.; Bannwarth, C.; Caldeweyher, E.; Pisarek, J.; Hansen, A. A General Intermolecular Force Field Based on Tight-Binding Quantum Chemical Calculations. *J. Chem. Phys.* **2017**, *147*, 161708.
- (97) Grimme, S.; Bannwarth, C.; Shushkov, P. A Robust and Accurate Tight-Binding Quantum Chemical Method for Structures, Vibrational Frequencies, and Noncovalent Interactions of Large Molecular Systems Parametrized for All spd-Block Elements (Z = 1–86). *J. Chem. Theory Comput.* **2017**, *13*, 1989–2009.
- (98) Bannwarth, C.; Ehlert, S.; Grimme, S. GFN2-xTB—An Accurate and Broadly Parametrized Self-Consistent Tight-Binding Quantum Chemical Method with Multipole Electrostatics and Density-Dependent Dispersion Contributions. *J. Chem. Theory Comput.* **2019**, *15*, 1652–1671.
- (99) Tsuzuki, S. CH/ π Interactions. Annu. Rep. Prog. Chem., Sect. C: Phys. Chem. **2012**, 108, 69–95.
- (100) [6] CPP was excluded from this study as only a statistically not representative number of adsorption events; e.g., two *p*-xylenes in four unit cells, were observed.
- (101) Baker, K. N.; Fratini, A. V.; Resch, T.; Knachel, H. C.; Adams, W. W.; Socci, E. P.; Farmer, B. L. Crystal Structures, Phase Transitions and Energy Calculations of Poly(p-Phenylene) Oligomers. *Polymer* **1993**, 34, 1571–1587.